Expanding the role of impurity spectroscopy for investigating the physics of high-Z dissipative divertors

M.L. Reinke [a,*], A. Meigs [e], E. Delabie [a], R. Mumgaard [b], F. Reimold [c], S. Potzel [d], M. Bernert [d], D. Brunner [b], J. Canik [a], M. Cavedon [d], I. Coffey [f], E. Edlund [b], J. Harrison [e], B. LaBombard [b], K. Lawson [e], B. Lomanowski [g], J. Lore [a], M. Stamp [e], J. Terry [b], E. Viezzer [d], the ASDEX Upgrade Team, the Alcator C-Mod Team, and JET Contributors[1]

[a] Oak Ridge National Laboratory, Oak Ridge, TN 37831, USA
[b] Plasma Science and Fusion Center, Massachusetts Institute of Technology, Cambridge, MA 02139, USA
[c] Forschungszentrum Jülich GmbH, 52425 Jülich, Germany
[d] Max-Planck-Institut für Plasmaphysik, Boltzmannstr. 2, 85748 Garching, Germany
[e] CCFE, Culham Science Centre, Abingdon, Oxon, OX14 3DB, UK
[f] Queen's University, Belfast, BT7 1NN, Northern Ireland, UK
[g] Aalto University School of Science, Department of Applied Physics, P.O. Box 11100, FI-00076 AALTO, Finland

ARTICLE INFO

ABSTRACT

New techniques that attempt to more fully exploit spectroscopic diagnostics in the divertor and pedestal region during highly dissipative scenarios are demonstrated using experimental results from recent low-Z seeding experiments on Alcator C-Mod, JET and ASDEX Upgrade. To exhaust power at high parallel heat flux, $q_\parallel > 1$ GW/m^2, while minimizing erosion, reactors with solid, high-Z plasma facing components (PFCs) are expected to use extrinsic impurity seeding. Due to transport and atomic physics processes which impact impurity ionization balance, so-called 'non-coronal' effects, we do not accurately know and have yet to demonstrate the maximum $q_\parallel$ which can be mitigated in a tokamak. Radiation enhancement for nitrogen is shown to arise primarily from changes in Li- and Be-like charge states on open field lines, but also through transport-driven enhancement of H- and He-like charge states in the pedestal region. Measurements are presented from nitrogen seeded H-mode and L-mode plasmas where emission from N^{1+} through N^{6+} are observed. Active charge exchange spectroscopy of partially ionized low-Z impurities in the plasma edge is explored to measure N^{5+} and N^{6+} within the confined plasma, while passive UV and visible spectroscopy is used to measure N^{1+}-N^{4+} in the boundary. Examples from recent JET and Alcator C-Mod experiments which employ nitrogen seeding highlight how improving spectroscopic coverage can be used to gain empirical insight and provide more data to validate boundary simulations.

1. Introduction

The importance of being able to reach and sustain the detached divertor regime is a fundamental challenge of transferring the present successes of high-power, short pulse high-Z diverted tokamaks to ITER and beyond. Future devices will have parallel heat fluxes of multiple GW/m^2 which rival and exceed capabilities of present devices. Pulse lengths will increase, making long-term erosion and dust production increasingly important. In this paradigm, the zero or low-erosion divertor becomes a necessity which requires divertor temperatures to fall below the sputtering threshold of tungsten. While advances in magnetic topology and divertor geometry may offer new means of optimization, it is envisioned that extrinsic impurity seeding will be required to exhaust power on open field lines prior to reaching plasma facing components (PFCs), reducing the divertor temperature to levels either below the sputtering threshold or enabling momentum loss processes which lead to pressure loss and detachment. Impurity seeding cannot be applied indiscriminately to achieve desired PFC

conditions, as excessive seeding has been demonstrated to lead to degradation of confinement and increased disruptivity. Examples of achieving favorable divertor and PFC conditions are possible with existing tools which characterize the plasma surface and total radiated power, [1–5], but it is less clear if present diagnostics are sufficient to understand the physics which limits radiative exhaust. Following an extensive body of prior work characterizing carbon emission in devices with CFC/graphite PFCs, recent work on the high-Z diverted tokamaks ASDEX Upgrade, JET and Alcator C-Mod has focused on improving spectroscopic observations of extrinsically seeded impurities, such as nitrogen, neon, argon and krypton. This research outlines the motivation for improving spectroscopic coverage for non-intrinsic seeded impurities and shows examples of implementing new methods in H-mode and L-mode plasmas.

Section 2 discusses radiative exhaust by impurities and the importance of distortions to equilibrium ionization balance, so-called non-coronal radiation, and how such information is encoded in a range of charge states for low-Z impurity emission. Section 3 describes ways to enhance charge state observation, with coverage that has been demonstrated on Alcator C-Mod, JET and ASDEX-U which utilizes present UV/visible diagnostics. Section 4 demonstrates these techniques in dissipative L-mode and H-mode plasmas that use heavy N_2 seeding while Section 5 discusses the role these techniques could play in future boundary validation studies and feedback control.

2. Background

Many authors have discussed methods to estimate the maximum radiation possible on open field lines by integrating the electron energy balance along an open field line at fixed pressure [6–8]. While not appropriate for judging degree of detachment, this model allows assessment of the impurity levels necessary to achieve lower power flux as well as reach low temperature where momentum loss processes are known to increase.

$$q_\parallel^2(T) = q_{\parallel,u}^2 - \int_{T_u}^T 2\kappa_0 p_u^2 f_z L_Z(T')\sqrt{T'}dT' \qquad (1)$$

Here $q_\parallel(T)$ is the parallel heat flux as a function of downstream temperature, with $q_{\parallel,u}$ being the upstream heat flux, κ_0 collects constant terms in the parallel heat conductivity, p_u is the upstream pressure, f_z is the impurity fraction and L_Z captures the radiating efficiency, the so-called 'cooling-curve'. While this equation computes what reduction in heat flux is possible as temperature is reduced, another constraint, the sheath heat flux transmission, $q_{sh} = \gamma nT^{1.5}$ must be included to specify the $(T, q_\parallel)$ achieved. A sheat heat flux transmission factor of $\gamma = 8$ is used, as outlined in Section 2.8 of [9]. As can be seen from (1), at fixed upstream pressure, to decrease the target heat flux requires increasing the integrand by either increases the level of impurities, f_z, or increasing the width in temperature of L_Z. This can be done by mixing multiple impurities together, but the limit of a single impurity species to act is influenced by its residence time in the plasma, τ, and electron density, n_e. Increasing the product, $n_e\tau$ allows impurities to reach their equilibrium ionization distribution, as discussed in [10], changing the charge state distribution and thus the radiative efficiency, L_Z when summed over all charge states. While colloquially referenced as 'non-coronal radiation', the $n_e\tau$ ansatz is one way to highlight a wider range of physics that includes charge-exchange recombination and cross-field transport. In this context, we use it to motivate improved spectroscopic coverage which can then be interpreted using more sophisticated boundary transport codes.

Using data from [11], the f_z for various impurities necessary to achieve a 5 eV target temperature at can be calculated as $n_e\tau$ is varied. Here $q_{\parallel,u} = 1$ GW/m² upstream parallel heat flux, $n_u = 1.0 \times 10^{20}$ m⁻³ and parallel connection length $L_\parallel = 30$ m (neces-
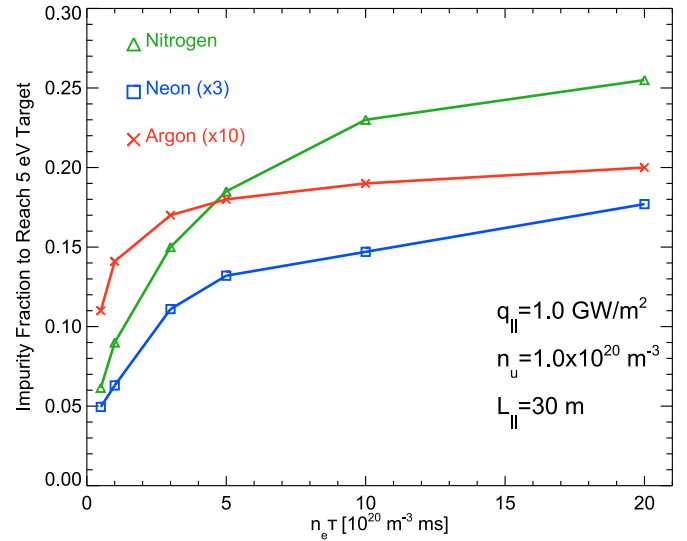

Fig. 1. Estimation of impurity fraction necessary to reduce the temperature of a flux tube with given $q_\parallel$, n_u and $L_\parallel$ as $n_e\tau$ is varied.

sary to compute T_u via the two-point model) are used. This is shown in Fig. 1, where it is apparent the increased fraction of nitrogen needed to reduce the target T_e relative to neon and argon, and the dramatic reduction of f_z possible if $n_e\tau$ can be reduced to less than 1.0×10^{20} m⁻³ms.

Given the importance of these radiation enhancements, it's important to have sufficient experimental measurements to capture the effect for modeling or empirical investigation. Varying $n_e\tau$, the non-equilibrium cooling curves can be investigated for other impacts than just the total radiated power. Using ADAS406 [12], the evolution of the ionization balance during the residence time τ is calculated for $n_e = 1.0 \times 10^{20}$ m⁻³ at each T_e for a range of $0 < \tau < 100$ ms. The cooling-curve, L_Z, is computed by dividing the time-integrated power loss by the τ. The excitation and photon emission mechanisms, for the most part, are not influenced by the finite time scales discussed here, so the standard charge-state resolved cooling curves are used: plt96_n.dat and prb96_n.dat available via OPEN-ADAS (http://open.adas.ac.uk/). In Fig. 2a, the total cooling-curve is plotted for $n_e\tau = 0.1$, 1.0 and 10.0×10^{20} m⁻³ ms. In Fig. 2b, the charge-state resolved L_Z data are plotted versus ionization stages for N^{0+} (N-like) to N^{7+} (fully-stripped) for three different electron temperatures. At low temperature, $T_e = 10$ eV and below, there is no difference in the cooling curves, but there is a clear redistribution of charge states, with the peak losses coming from Be-like and Li-like nitrogen at $n_e\tau = 10.0$, while this shifts to B-like at $n_e\tau = 0.1$. These charge states have a relatively similar radiating efficiency, so there is no change in L_Z, although changing the charge state would impact the sputtering rate. At higher temperatures there is an increasingly larger separation of the cooling curves as $n_e\tau$ is decreased which is driven by the enhancement of Li-like and Be-like nitrogen. At higher $n_e\tau$, these charge states are exchanged for He-like nitrogen, which weakly radiates since it takes much higher temperatures to excite the ground state electron in the closed shell ion compared to ionizing the remaining valence electron from Li-like charge state. This shows the benefit of measuring full range of emitting charge states, N^{0+}-N^{4+} within the 2D, or possibly 3D, boundary plasma to help ensure the full range of physics that leads to radiation enhancement can be understood.

A similar effect happens to neon, but shifted to higher temperatures, with boundary emission spread over a wider range of ionization stages, from neutral to Ne^{7+} (Li-like). Similarly for Ar, boundary emitters affected by non-equilibrium processes are neutral to
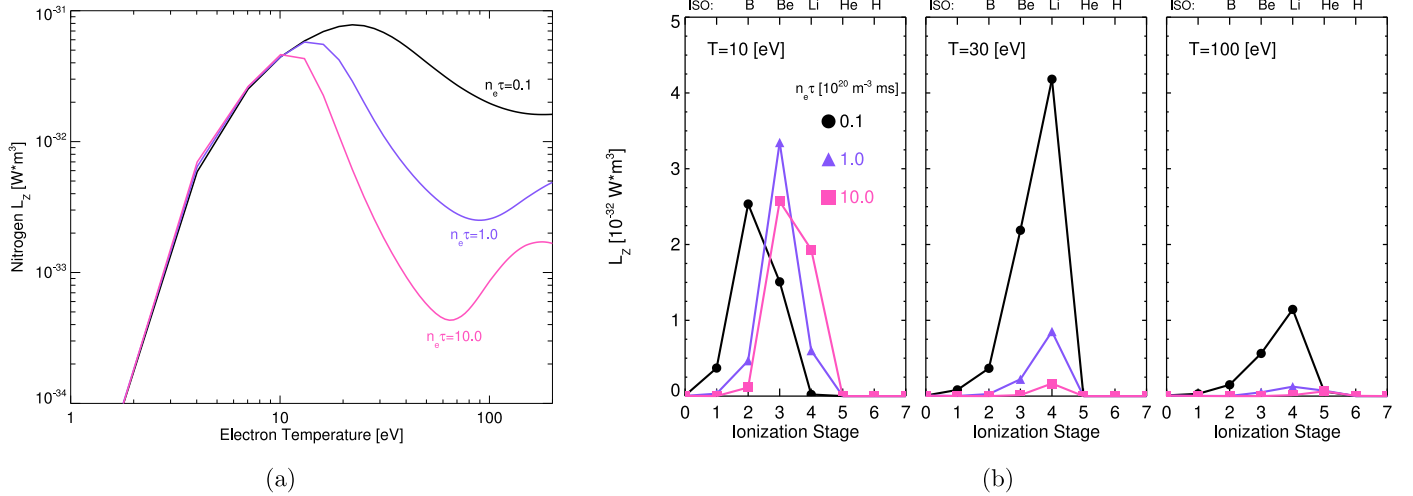
Fig. 2. (a) Demonstration of the enhancement of nitrogen radiation for ions out of ionization equilibrium, showing a large increase in L_Z as $n_e\tau$ is reduced and (b) how this enhanced radiation is distributed among different ionization stages.

Ar^{7+} (Na-like), with Ne-like Ar acting as the weak, closed-shell radiator. Similar arguments for Kr indicate that Ni-like Kr would be the first closed-shell meaning boundary emission should be spread from neutral (Kr-like) to Kr^{7+} Cu-like. Both neon and nitrogen share similar, well understood isoelectronic sequences, while moving to Ar and Kr increases the challenge of being able to accurately model the atomic physics process in weakly ionized mid and high-Z impurities. Line emission for partially ionized noble gas species is also more widely distributed into the deep UV range down to 200 nm making it more challenging to measure.

While at low temperatures nitrogen, neon and argon are all efficient radiators, the well-known complication with their excessive use is that increasingly higher-Z impurities will also radiate at temperatures achieved in the pedestal of present devices, $T_e <$ 1 keV. It is not yet clear where the demarcation is relative to the pedestal top and separatrix between regions which have a negative impact, such as reducing normalized energy confinement despite also reducing divertor heat flux. Importantly, in future devices like ITER, the pedestal temperature will increase substantially while the divertor temperatures will be similar. For edge transport barriers that feature strong density gradients, large inward neoclassical impurity flux is observed, and in the pedestal region, between ELMs, neoclassical processes are thought to dominate [13]. This makes understanding the interplay between Z-dependent transport physics and Z-dependent atomic physics important in translating present results to future reactors. This inward convection is another process which can alter the charge state distribution and increase the radiating efficiency of the impurities by pulling partially ionized charge states which normally might exist at the bottom of the temperature pedestal to higher temperatures and densities, increasing their radiating efficiency. To demonstrate this effect, EDA H-mode profiles, described in [14] are used in STRAHL [15] simulations with a range of inward convection. Input data are shown in Fig. 3, where the particle diffusivity is reduced throughout the pedestal to levels near neoclassical predictions and an inward convective layer near the steep density gradient region is scanned from zero to -100 m/s. For large negative convection, the combined H- and He-like charge state fractions are nearly eliminated for $r/a > 1.0$, but more weakly reduced inside the plasma. In contrast, the Li- and Be-like charge states which only exist for $r/a >$ 1.0 are strongly reduced. This has the effect of redistributing the radiative loss relative to the electron temperature pedestal, demonstrated in Fig. 4 for both neon and nitrogen. The total emissivity profiles derived from the STRAHL output as a function of minor
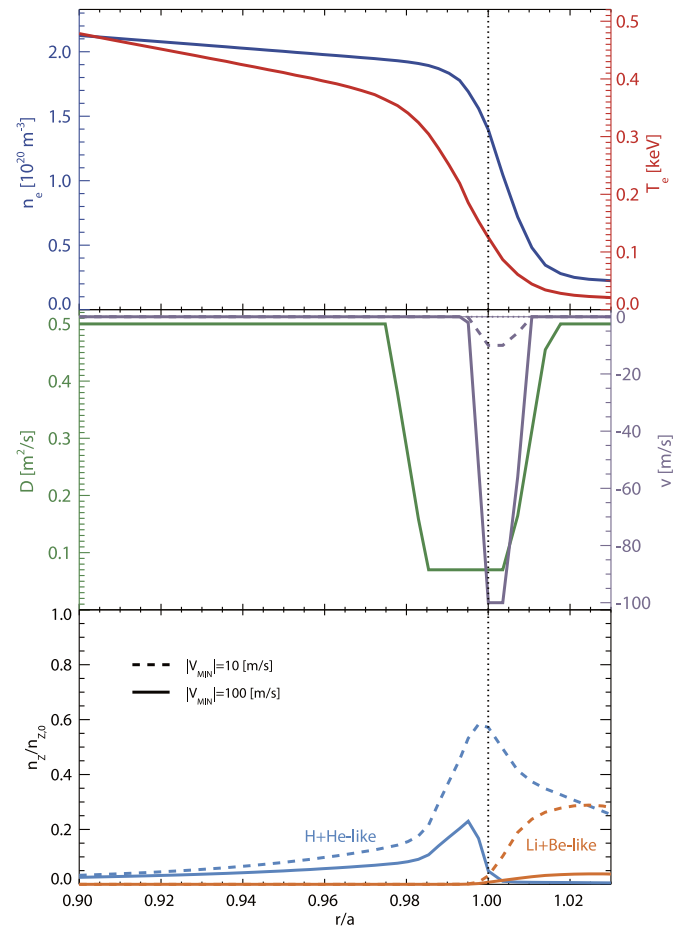

Fig. 3. (top) STRAHL input T_e and n_e profiles with (middle) diffusion and convection profiles estimated to model an edge transport barrier. A limited range of charge state density profiles (bottom) are plotted for two possible peak convection values.

radius are integrated over the volume to derive radiated power, assuming a 1D, circular model with $dV = 4\pi^2 R_0 r dr$ for simplicity. The core radiated fraction is found by integration from on-axis to $r/a = 0.96$ and normalizing this to the integral out to the edge of the simulation grid, including the radiating SOL. As convection is increased, the fraction of power lost radially inside of the pedestal
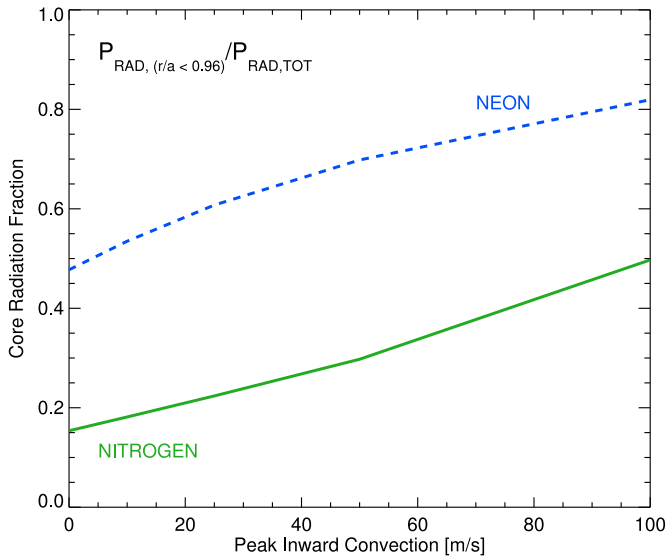
Fig. 4. Resulting change in spatial structure of the 1D radiation profile computed from STRAHL simulations, showing an inward shift of radiation as convection is decreased to −100 m/s.

top is enhanced. The level of change from ignoring the convection at levels close to neoclassical predictions is significant even for nitrogen and is similar to change that would be observed from switching to neon and ignoring convection. This makes measuring N^{5+} (He-like) and N^{6+} (H-like) charge state density profiles inside the separatrix important to constraining this effect when simulating boundary radiation.

3. Spectroscopic methods

The mechanisms discussed in Section 2 highlight a need to increase the spatial coverage of charge states between source terms and fully-stripped species. This section discusses a methodology to do this, taking into account the realities of diagnostic integration and operation on the JET, Alcator C-Mod and ASDEX Upgrade tokamaks. For purposes of simplicity and to link to the majority of experimental data, the focus will be placed on nitrogen, although similar work on neon, argon and krypton is currently in progress. Figures and text utilize spectroscopic notation when referencing line emission, which utilizes roman numerals at values one higher than the ionization stage, i.e. N V is from N^{4+} (Li-like).

The ideal means to convincingly measure partially ionized charge states of low-Z impurities is through dipole transitions responsible for the dominant power loss. For N VII (H-like) and N VI (He-like) these are the n = 2-1 transitions in the soft x-ray (SXR) region over $2 < \lambda < 3$ nm, and for N V (Li-like) to N III (C-like) these are the n = 2-2 and n = 3-2 transitions in the vacuum ultraviolet region (VUV) in the $20 < \lambda < 130$ nm range. This creates a significant challenge to try and observe spatial profiles of these lines as diagnostics which observe these wavelength ranges cannot use refractive optics and have limited use of reflective optics. While wide spectral range, single chord spectrometers like SPRED [16] and XEUS/LoWEUS [17] are widely used, imaging spectrometers in this spectral range are more limited. While they have been demonstrated using transmission gratings [18] and imaging spectrometers [19], these are not operational on present high-Z devices. On JET, a spatially scanning single chord VUV spectrometer exists [20] and ones previously existed on C-Mod [21] and AUG [22]. The JET system has limited spectral coverage, allowing 3–4 lines to be observed per discharge and C-Mod spectrometer required multiple, repeated shots to obtain spatial profiles making both experi-
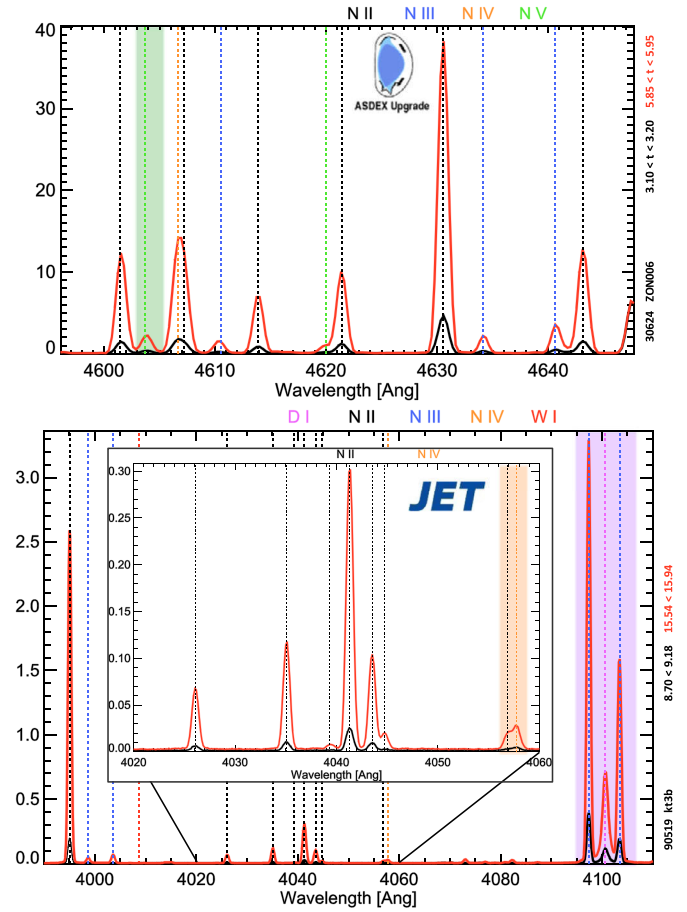

Fig. 5. Measured spectra from boundary plasma showing ranges to observe N V (top) and N II-IV (bottom). High resolution is required to avoid overlap with D I and N II lines for N III, N IV and N V. Note that spectra are plotted versus angstroms while line positions are given in nanometers in the next.

mentally inefficient to capture the spatio-temporal evolution from a wide range of charge states.

This has motivated a recent push to expand the utilization of existing visible and ultraviolet spectroscopy tools to observe these charge states. This is already a common approach for carbon devices and much of what was accomplished follows from prior successes such as those on JT-60U [23,24] and DIII-D [25,26] where enhanced coverage was explored. The n = 3-3 transitions in N II through N V happen to emit between $340 < \lambda < 720$ nm. These transitions are heavily utilized by the astrophysics community to observe and characterize Type O stars [27,28] and comprehensive lists can be found in [29,30] some of which are included in digital format in NISTs ASD, an invaluable tool for these investigations. While these transitions can be observed using in-air instruments, complications exist in how they are measured in practice. A much more comprehensive description of the spectral ranges explored on AUG, C-Mod and JET will be presented elsewhere, with important results summarized here. Fig. 5 shows examples of the N II through N V transitions observed in recent JET and AUG experiments. For Li-like nitrogen, the N V 3p-3s lines exist very close to strong N II 3p-3s multiplet, requiring high resolution rather than survey instruments to resolve them. The strong 3p-3s triplet in N IV, the analog of the widely used ~465 nm C III triplet, is at ~347 nm. While this is well isolated from contamination, it is below where standard glass optics transmit, thus high-throughput imaging spectrometers which utilize commercial SLR lenses cannot observe them. The weaker 3d-3p line is ob-
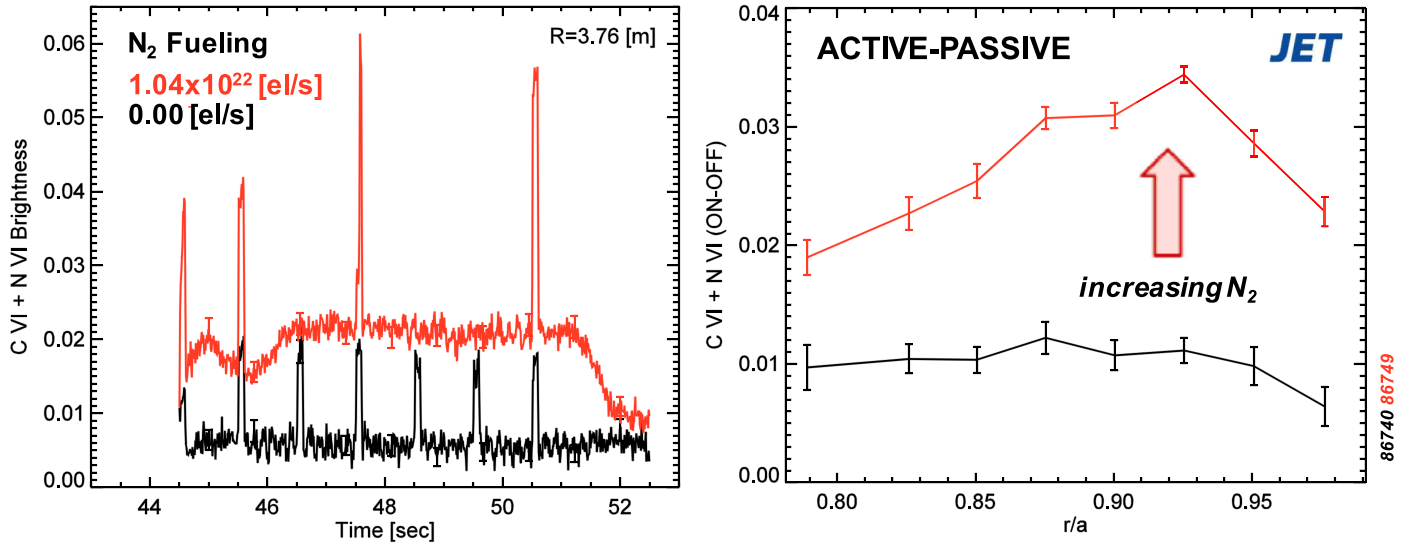
Fig. 6. Demonstration of active and passive N VI charge exchange showing enhancement during NBI (left) and the transition from C VI dominated to mixed N VI and C VI emission profile (right).

served at 405.78 nm, but this is contaminated by a N II line, as shown in the inset in Fig. 5. The strong 3p-3s N III doublet brackets the n = 6-2 transition in hydrogen and its isotopes, requiring a high resolution instrument to distinguish all three, especially under strong Stark broadening. In general, 3p-3s N II lines are strong and well resolved in spectral ranges optimized for N III-V coverage. An additional benefit of exploiting spectroscopy in exhaust scenarios is that normally weak lines have high signal to noise, as shown in the inset in Fig. 5. Due to the combined need to cover wide spectral ranges with high resolution, simultaneously observing this full range of nitrogen charge states requires either repeated discharges or multiple spectrometers which use beam splitting optics to extend observations over the same set of chords. The spectral ranges displayed in Fig. 5, along with coverage of the N IV triplet at ∼347 nm are recommended as a minimum set of observables necessary to capture the boundary radiating charge states.

For confined plasma and pedestal region, additional measurement techniques must be used. Radial profiles of N V have been measured in the midplane separatrix region on AUG as part of this work, but characterizing the spatial extent of H-like and He-like nitrogen when limited to UV/visible tools requires charge exchange recombination spectroscopy (CXRS). Existing optical systems on JET [31] and Alcator C-Mod [32] have been used to measure active CXRS of partially ionized charge states of nitrogen and neon. While CXRS traditionally uses fully-stripped impurities in an effort to measure flow and temperature over the plasma cross-section, it can be applied to partially ionized charge states that exist near the edge plasma for low-Z impurities. CXRS uses $\Delta n = 1$ transitions at high-n which radiate in the visible, for example N VII n = 9-8 at 567 nm is emitted as a product of a charge exchange (C-X) reaction between injected neutrals and fully-stripped N^{7+}. The addition of an electron in the ground state creates a Rydberg like ion at a lower effective core charge which will emit at nearly identical wavelengths and similar efficiency as the equivalent fully-stripped state. For example, the $H^0 + N^{6+} = H^+ + N^{5+*}$ reaction will create excited states of N VI (He-like) with high-n transitions that have similar wavelengths as C VI (H-like). This has been noted in dedicated experiments [33,34]. It is necessary to substantially reduce the ionization stage away the equivalent hydrogenic reference, for example comparing Ne VII (Be-like) with N VII (H-like), in order to observe differences in wavelengths between high-n transitions in the former and the latter. This degeneracy is apparent in the

atomic physics rates as well [35], where the rate of excitation of the n = 8 level of N VI via C-X is nearly identical as the rate of excitation of n = 8 in C VI. This was calculated at center of mass collision energies relevant to neutral beams, both for ground state and $n = 2$ hydrogen neutrals. Additionally, this work suggests that at low energies, charge exchange of partially ionized species with $H^0(n = 2)$ continues to preferentially populate the excited states resulting in visible transitions, allowing both neutral beam and gas puff charge-exchange [32] to be utilized. For divertor plasmas, population by C-X is an important tool to highlight the encroachment of the high neutral density/recombination zone into the confined plasma, as discussed in Section 4.

Experiments on JET and Alcator C-Mod have investigated active CXRS with partially-ionized low-Z impurities and have demonstrated the ability to observe N^{5+} to N^{7+} and Ne^{8+} to Ne^{10+} at the outboard midplane of L-mode plasmas. In JET, a fixed grating spectrometer is used to measure C VI n = 8-7 emission at 529.0 nm in the edge region ($r/a > 0.8$) [31]. Neutral beam modulation is used to isolate the charge-exchange enhancement as the nitrogen content of the plasma is increased using divertor seeding, raising the level above a fixed intrinsic carbon background. Fig. 6 shows the time history of the 529.0 emission which is a combination of active and passive C VI and N VI. Prior to introducing nitrogen, the difference between the active and passive normalized to the passive is ∼2. At the highest level of N_2 injection, the passive and active emission are seen to increase by similar factors, maintaining a similar beam enhancement, indicating the nitrogen has similar charge-exchange efficiency as fully-stripped carbon, qualitatively demonstrating results from [35]. Also shown in Fig. 6 is the change in shape of the radial profile of active minus passive emission, which is expected to translate to a similar change in the charge state density profiles derived from a more detailed CXRS analysis. Before nitrogen seeding, the emission is flat out to $r/a = 0.95$, consistent with a fully-stripped profile while at the highest level of nitrogen seeding, the profile is hollow, exhibiting a peak between $0.9 < r/a < 0.95$, consistent with a 'shell' of the H-like nitrogen.

Motivated by these results, dedicated gas-puff charge exchange scoping studies have been completed on Alcator C-Mod. Fiber views from a poloidally viewing edge viewing poloidal periscope observing $0.85 < r/a < 1.02$ were routed into a Chromex 500is imaging spectrograph. Neutral deuterium was injected by a capillary system into the low-field edge and the interaction region
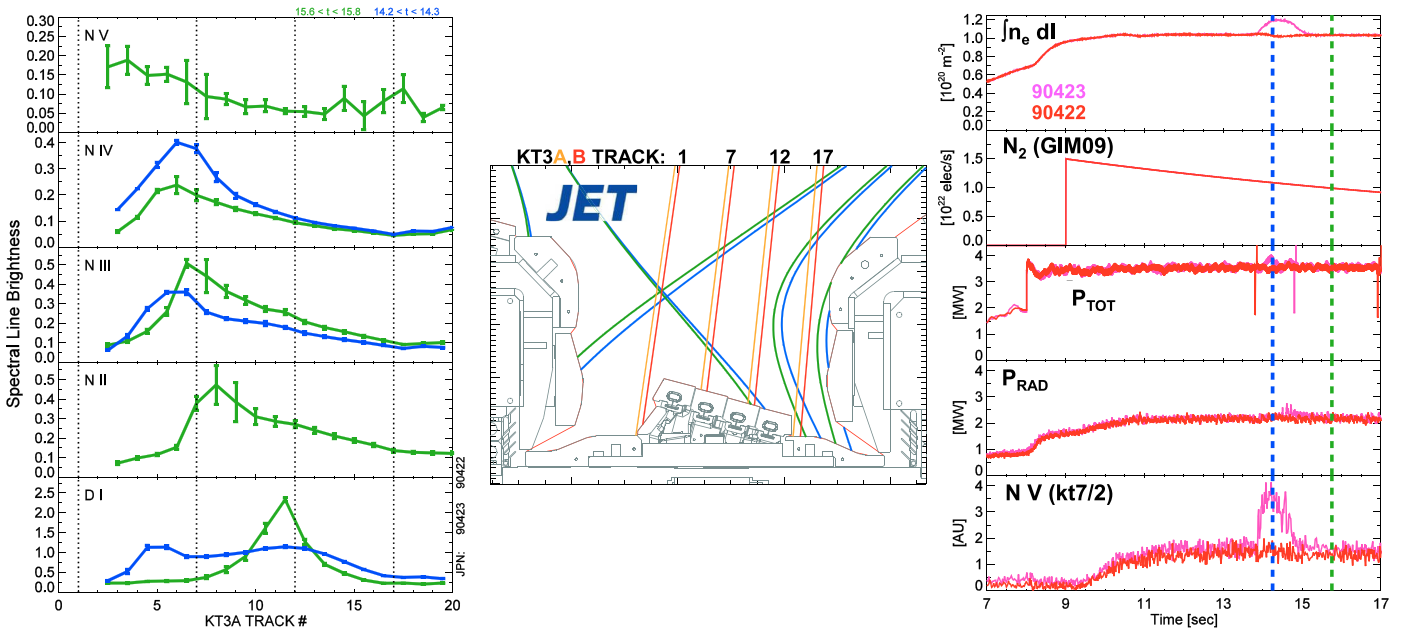
Fig. 7. Example of enhanced spectroscopic tools used in JET L-mode experiments. Spatial profiles of D I and N II-V (left) are shown for chords viewing across the outer divertor (middle) at two different time points in repeated discharges that employed a weak strike point scan (right).

observed, as described in [32]. In an Ohmic plasma, emission at wavelengths that would correspond to high-n transitions from Ne X, F IX, O VIII and N VII, C VI and B V were observed before and after main-chamber injection of neon and nitrogen, respectively. In both cases, spectral emission corresponding to active C-X off of fully-stripped, H-like and He-like charge states were observed for both impurity species well above continuum and intrinsic levels of impurities. Further work is necessary to utilize these measurements quantitatively, but results from JET and C-Mod clearly show an ability to measure these charge states via active spectroscopy.

4. Experimental examples of boundary spectroscopy

The enhanced boundary spectroscopic capabilities have been applied to a range of dissipative divertor studies on JET, ASDEX Upgrade and Alcator C-Mod during the 2014–2016 operational campaigns. Much work remains to analyze and extract data from all spectroscopy tools and this section describes a selection of observations made at JET and Alcator C-Mod that highlight changes in the spatial structure of emission from various nitrogen charge states. Complementary work on using data to extract n_e, T_e and/or p_e from line ratios is on-going as well.

4.1. JET

Recent L-mode and H-mode experiments on JET explore regimes of heavy seeding in order to improve empirical understanding of DEMO-relevant power exhaust and to provide data sets to be used for validation of boundary modeling. New experiments in high density L-modes with line-integrated n_e $\sim 10^{20}$ m^{-2} extend prior work at low density [36] and initial results relating to improved spectroscopic coverage are shown in Fig. 7. A decreasing, feed-forward N_2 at rates above 10^{22} el/s is injected into the common flux region of the outer divertor, leading to a stationary high-recycling, nitrogen seeded L-mode. This discharge is repeated to allow for a wider survey of impurity spectroscopy and imaging setups in order to increase the amount of data available for comparison with boundary modeling simulations. In both discharges, between $13.0 < t < 14.0$ s, the divertor geometry was scanned

slightly to improve diagnostic coverage of fixed Langmuir probes. This difference in geometry is observable in the magnetic geometry shown in Fig. 7. For reasons presently unknown, an x-point MARFE was formed transiently during JET pulse number 90423 but not the previous discharge, 90422, despite both having the same density, N_2 seeding, input power and radiated power. In cases with higher N_2 seeding, formation of the MARFE was quickly followed by a disruption.

JET has a substantial number of divertor spectroscopy tools, and these initial observations focus on the utilization of a portion of the capabilities of the mirror link divertor spectrometer, KT3 [37,38]. Lines of sight are shown in Fig. 7 over the magnetic equilibrium and measurements from KT3A and KT3B, two 0.75 m imaging Czerny-Turner spectrometers which can be scanned to cover 200–660 nm and 390–750 nm, respectively. Newtonian telescope optics and dichroic beam splitters which transfer light from the tokamak to the remote spectrometers results in shifting of the views of the two instruments. Measurements are plotted in KT3A line of sight, which ranges from the X-point at low track number past the outer target, with KT3B shifted 1/2 a channel relative to KT3A. Repeated discharges are used to cover the spectral regions shown in Fig. 5 and beyond. The lines plotted in Fig. 7 correspond to D I n = 6-2 at 410.0 nm and 3p-3s transitions for N II at 399.5 nm, N III at 409.7 nm, N IV at 347.9 nm and N V at 460.37 nm. During the stationary phase of the L-mode, shown in green, the charge state emission layers are progressively separated moving away from the outer target where the D I emission is localized. While no radially viewing chords are available to aid in localization, a likely interpretation is that this emission is spread across the outer leg in flux tubes near the separatrix. During the MARFE phase, shown in blue, the spatial structure of the spectroscopic emission changes dramatically. The D I emission profile becomes very broad, the N III profile shifts towards the x-point but reduces in intensity while the N IV emission increases. Coverage of N II and N V were not available for comparison, but other L-modes during this session which resulted in MARFE formation prior to disruption showed a large increase in the N V emission. Initial examination of H-mode plasmas, not shown here, also show a significant increase in N V, nearly and order of magnitude, in contrast to factors of x2
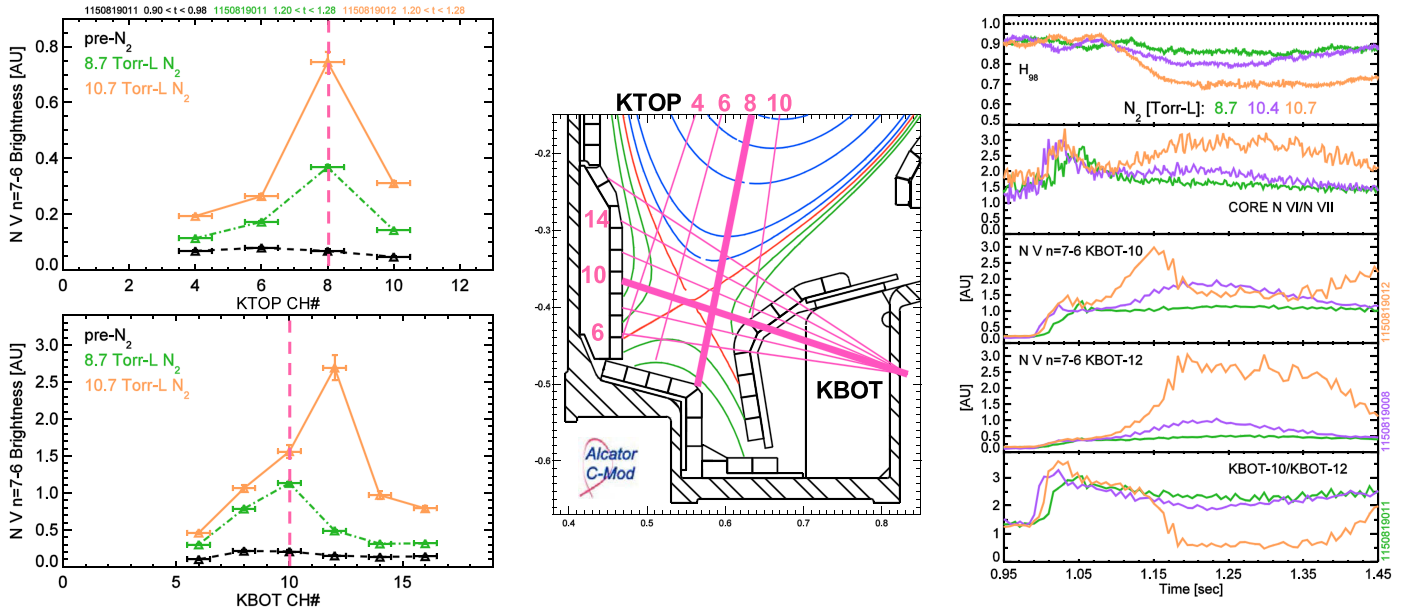
Fig. 8. Example of spectroscopic methods implemented at Alcator C-Mod where spatial profiles of N V n = 7-6 emission in the divertor are tracked as private flux nitrogen fueling is increased shot-to-shot. Movement of emission layers is shown to follow confinement degradation.

to x3 for N II-IV. These observations are consistent with the background discussion in Section 2 that highlights the importance of the Li-like charge state in driving the peak radiation losses.

4.2. Alcator C-Mod

Ongoing work at Alcator C-Mod is investing the limits of high performance dissipative divertors in the conventional x-point, vertical target configuration. While earlier work [4] demonstrated the compatibility of Ne and N_2 seeding with H_{98} ~1 operation in the partially detached regime, new experiments push low-Z seeding further to examine pronounced to full detachment. Using the private flux capillary fueling system, nitrogen was introduced into stationary 800 kA, 5.4 T EDA H-mode plasmas, increasing the total gas injected over a ~500 ms timescale shot to shot from 8.7 to 10.7 Torr-L. Prior to injection, surface heat fluxes of ~15 MW/m^2 and temperatures of $25 < T_e < 30$ eV were measured at the strike point. All seeding levels reduced the divertor heat flux to zero within the uncertainty of the surface thermocouples (1–2 MW/m^2) and strike point temperatures below 10 eV, with increasing N_2 expanding the spatial extent of detachment at the outer target. Increasing seeding also resulted in a drop in stored energy, as shown by the decrease in H_{98} in the time history plots in Fig. 8. Spectroscopic tools are used to characterize changes in the volumetric impurity emission as the nitrogen seeding is raised and the negative impacts on the core plasma are observed. Ten lines of sight, with a mix of radial as well as vertical views, as shown in Fig. 8 are input into fixed Volume Phase Holographic grating Kaiser spectrometers typically used for CXRS, measuring B V emission in the pedestal region at $\lambda \sim 494$ nm [39]. When viewing the divertor during N_2 seeding recombination radiation from He-like to Li-like nitrogen is strongly observed, the result of radiative recombination and C-X with background neutrals, as the n = 7-6 N V transition can be populated at low temperatures from C-X via $H^0(n=2)$, similar to C-X with fully-stripped boron producing n = 7-6 emission in B V. Additional to these views, but not discussed here, are 16-channels that view $380 < \lambda < 413$ nm, which includes the n = 6-2 through n = 9-2 Balmer lines as well as N II, N III and N IV lines discussed above. These views are interleaved with those shown in Fig. 8.

Fig. 8 shows the line brightness of emission at 494.4 nm, a combination of B V and N V emission as discussed in Section 3 for C VI and N VI. Prior to seeding the signal is weak, indicating that there is little B V contribution to the measurement, allowing the data to be used to track the location of the recombination layer of He-like to Li-like nitrogen. Along a flux tube, this should then precede the radiation layer which is driven by L-shell nitrogen charge states responsible for dropping the target T_e. This is useful to pair with the neutral deuterium emission, with the two bounding the radiating volume and could be used to explore the expansion or contraction of the radiating volume as magnetic topology and geometry is varied. The lines of sight corresponding to peak emission for the 8.7 Torr-L N_2 injection shot are highlighted in bold in Fig. 8. As the seeding is increased, the peak emission moves to a higher radial channel on KBOT, while maintaining the same emission region on the vertical KTOP channels. Within present spatial resolution limits, this suggests a movement of the He-like recombination layer along open field lines. The localization on KBOT 6→ 10 suggest at lower seeding, the emission is along on the outer divertor leg. As seeding is increased, the emission moves up to KBOT 12→ 16, consistent with moving up the SOL above the X-point or possibly even inside the confined plasma.

Fig. 8 also shows time histories of various spectroscopic data over the N_2 fueling scan. Here the stored energy drop with increased nitrogen is characterized by a drop in normalized energy confinement, H_{98}. Measurements of H-like (N VII n = 3-1 at 2.09 nm) and He-like (N VI n = 2-1 at 2.91 nm) nitrogen from the midplane radial view of a VUV spectrometer are plotted alongside the N V emission measured on two KBOT chords which see the emission layer movement. At lower seeding levels, when H_{98} is not perturbed, the nitrogen emission remains stationary, and the structure, characterized by the ratio of the two measurements, is nominally constant. As the seeding is increased and confinement is impacted, the N VI/N VII SXR emission ratio is evolving continuously. This is likely due the drop in pedestal temperature which is what is driving the stored energy drop reduction, but it highlights a possible self-reinforcing behavior. In contrast, while the levels of the N V emission on both KBOT channels increase as the H_{98} drops, it is not until the confinement stops decaying at the KBOT 10/12 ratio goes through at significant step change at t ~1.15 s in shot

number 1150819012. For t > 1.35 s on 1150819012, the capillary fueling system is starting to reduce the instantaneous N_2 fueling rate allowing the confinement to begin to recover and the N V recombination radiation shifts back down, although the full confinement recovery lags this transitions. This suggests, but does not prove, that the confinement drop is a response to increased radiation loss at a nominally fixed pattern, and that the movement of the He-like nitrogen recombination layer follows this. Further progress and future investigations will connect these measurements with wider observations of spectroscopic and radiated power measurements in the divertor.

5. Discussion

Previous sections demonstrated the opportunities for new insights into divertor experiments possible with improved spectroscopic utilization, and this section discusses where these approaches could have impact. Approaches using present fluid boundary modeling tools such as SOLPS [40] and UEDGE [41] requires 'tuning' of the spatially varying cross-field transport to match measured fluid profiles, but this is typically done using electron density and temperature measured upstream and at the target. Some inclusion of impurity emission has taken place [42], but tailoring of the cross-field diffusivities for each charge state to try and match total radiation from bolometry and impurity spectroscopy has not yet been attempted. We know from experiments that there are turbulent structures in the divertor region [43,44] which may transport impurities differently than main-ions, so it should not be expected that a poloidally constant, species independent cross-field transport would be sufficient. Utilizing a wider range of charge state emission would help to capture the competition between cross-field and parallel transport and might provide insight into non-thermal corrections, all of which are required to accurately model the ionization imbalance discussed earlier and parameterized by $n_e\tau$. Ultimately both bolometry and the spatial profiles of charge states must be matched for the simulation to properly capture or model the physics responsible for setting the maximum radiated power from the boundary plasma. In the future, tools like XGC [45] and BOUT++ [46] should be used which attempt to model the cross-field transport in the edge plasma from first principles, and are now being improved to handle impurities in a manner necessary for exhaust studies [47,48]. This would transition the boundary validation community towards a similar methodology which has been successfully applied to understand the physics of core plasma transport [49]. First principles modeling tools, and cost-effective, flexible facilities to validate them at reactor-relevant $q_\parallel$ [50] are important to the investigation of alternative divertor geometries. Extrapolations to a reactor will be much larger for new concepts compared to the conventional x-point geometry due the latter being used on all large-scale devices. An, if not the, important utilization of improved spectroscopic coverage will be to demonstrate the physics of both the standard x-point and alternative geometries sufficiently well enough that reactor-scale devices can make informed design decisions on exhaust strategies.

While the value to improving boundary model validation is clear and requires additional work to fully exploit, it is argued that the spectroscopic methods will have less impact than other techniques being used for feedback control. It is not clear that spectroscopy captures what is important when using impurity injection, nominally maintaining a high pedestal temperature while eliminating or strongly reducing divertor erosion, with the reduction in target heat flux an expected consequence of erosion control. The possibility of using different combinations of impurities [51] results in a challenge to find and observe a suitable number of transitions with limited diagnostics. The variation in charge state balance with parallel heat flux creates a problem of interpretation. At lower $q_\parallel$, lower ionization stages become a more dominant power loss channel, thus different stages need to be tracked for robust control and a model developed to interpret measurements. Feedback control requires a negative outcome to be protected against, i.e. either some amount or location of specific charge state emission. While this can likely be found empirically in existing devices, this is difficult to translate between tokamaks and may be difficult to extrapolate to new facilities. Lastly, partially ionized charge states are responsible for the reduction in $q_\parallel$ and T_e but do not drive momentum loss, although more work investigating line ratios which can be combined to observe p_e variation could be relevant. In contrast bolometric or surface measurements may be more appropriate. They can be placed in absolute units, i.e. MW/m^2 for heat flux, which are of direct interest. Utilizing the magnitude of divertor radiated power is complicated because of the need to know and control the input power and core radiation, but the location of the divertor radiation peak, combining contributions from all the charge states, is likely to be more useful than individual charge state information. Target measurements from probes, current shunts or proxies using heat flux sensors, as well tracking the location of the hydrogenic recombination radiation are more closely related to detachment or measuring the low T_e at the target which is known to correspond to momentum loss [11]. Upstream measurements of the pedestal temperature provide direct information of the impact of seeding on the core.

Regardless of this outlook, long-pulse nuclear facilities will have severe restrictions to diagnostic access and compatibility making it ill-advised to down-select at this time. Optical diagnostics used in this work face challenges to mirror coatings and fiber-optics will be darkened. In this context, the VUV spectroscopy approaches should be re-evaluated, as first surface mirrors could be moved well away from the plasma and require small shielding penetrations, as shown by the D-T compatible systems on JET. In Fig. 8 it was shown how even a single radial view of the N VI and N VII charge states emitting in the pedestal region could be useful as a feedback signal, and this could be complemented by wide angle VUV views of the divertor. All tools still face the challenge of being used in control schemes that don't require substantial empirical tuning in exhaust plasmas that have a high risk of either disrupting due to over seeding or PFC damage due to underseeding.

6. Summary

Recent experiments on ASDEX Upgrade, JET and Alcator C-Mod are investigating the use of extrinsic impurity seeding to be used to mitigate heat fluxes to high-Z PFCs and reduce target temperatures to promote momentum loss processes. This work looks to understand the interconnected effects between edge and pedestal regions to understand the limitations of the radiative divertor looking forward to ITER and DEMO. Radiation enhancement due to multiple transport and reaction processes relevant to edge plasmas is critical to these scenarios and it is shown how measuring the individual charge states of the impurities can help provide a window into this effect. Active charge-exchange spectroscopy is demonstrated as a tool to measure H-like and He-like charge states inside the separatrix while passive ultraviolet and visible spectroscopy is used to measure the more weakly ionized, efficient radiators normally present on open field lines. Examples are given from Alcator C-Mod and JET impurity seeding experiments that demonstrate how improving spectroscopic coverage of extrinsic impurities can provide new information to help computational and experimental boundary physics research.

Acknowledgments

References

[1] J. Goetz, et al., Phys. Plasmas 3 (1908) 1996.
[2] M. Fenstermacher, et al., Phys. Plasmas 4 (1761) 1997.
[3] W. Fundamenski, et al., J. Nucl. Mater. 10 (2009) 390–391.
[4] A. Loarte, et al., Phys. Plasmas 18 (2011) 056105.
[5] A. Kallenbach, et al., Nucl. Fusion 55 (2015) 053026.
[6] K. Lackner, et al., Fusion Eng. Design 22 (1993) 107.
[7] D. Post, et al., J. Nucl. Mater. 1014 (1995) 220–222.
[8] A. Kallenbach, et al., Plasma Phys. Control. Fusion 55 (2013) 124041.
[9] P. Stangeby, The plasma boundary of magnetic fusion devices, Taylor and Francis, 2000.
[10] P. Carolan, V. Piotrowicz, Plasma Phys. 25 (1983) 1065.
[11] A. Kallenbach, et al., Plasma Phys. Control. Fusion 58 (2016) 045013.
[12] H.P. Summers, The adas user manual. Technical Report version 2.6.
[13] T. Pütterich, et al., J. Nucl. Materials 415 (2011) S334.
[14] R.M. Churchill, et al., Phys. Plasmas 22 (2015) 056104.
[15] R. Dux, Strahl user manual. Technical Report IPP 10/30, Max-Planck-Institut für Plasmaphysik.
[16] R.J. Fonck, et al., Appl. Opt. 21 (1982) 2115.
[17] J.K. Lepson, et al., J. Phys. B: Atom. Mol. Optic. Phys. 43 (2010) 144018.
[18] D. Kumar, et al., Rev. Sci. Instrum. 81 (2010) 10E507.
[19] T. Oishi, et al., Appl. Opt. 53 (2014) 6900.
[20] K.D. Lawson, et al., Rev. Sci. Instrum. 83 (2012) 10D536.
[21] J.E. Rice, et al., J. Phys. B: At. Mol. Opt. Phys. 29 (1996) 2191.
[22] U. Wenzel, et al., J. Nucl. Mater. 728 (1997) 241–243.
[23] T. Nakano, et al., J. Nucl. Mater. 255 (2009) 390–391.
[24] T. Nakano, et al., Nucl. Fusion 47 (2007) 1458.
[25] R. Isler, et al., Phys. Plasmas 4 (1997) 355.
[26] B. Zaniol, et al., Phys. Plasmas 8 (2001) 4386.
[27] J.G.R. Gonzalez, et al., Astron. Astrophys. 536 (2011) A58.
[28] J.G.R. Gonzalez, et al., Astron. Astrophys. 537 (2012) A79.
[29] C.E. Moore, Selected tables of atomic spectra, atomic energy levels and multiplet tables n iv, n v, n vi, n viia. Technical Report NSRDS-NBS 3, Section 4.
[30] C.E. Moore, Selected tables of atomic spectra, atomic energy levels and multiplet tables n i, n ii, n iii. Technical Report NSRDS-NBS 3, Section 5.
[31] Y. Andrew, et al., Rev. Sci. Instrum. 77 (2006) 10E913.
[32] R.M. Churchill, et al., Rev. Sci. Instrum. 85 (2013) 093505.
[33] L.J. Lemo, et al., Nucl. Instrum. Methods Phys. Res. B23 (1987) 101.
[34] E. Wolfrum, et al., J. Phys. B: At. Mol. Opt. Phys. 25 (1992) 2597.
[35] K. Igenbergs, et al., J. Phys. B: At. Mol. Opt. Phys. 45 (2012) 065203.
[36] L. Aho-Mantila, et al., J. Nucl. Mater. 438 (2013) S321.
[37] A. Meigs, et al., Rev. Sci. Instrum. 81 (2010) 10E532.
[38] B.A. Lomanowski, et al., Rev. Sci. Instrum. 85 (2014) 11E432.
[39] R. McDermott, Edge Radial Electric Field Studies Via Charge Exchange Recombination Spectroscopy on the Alcator C-Mod Tokamak, Massachusetts Inst. of Tech., 2009 Phd thesis.
[40] R. Schneider, et al., Contrib. Plasma Phys. 46 (2006) 3.
[41] T.D. Rognlien, et al., J. Nucl. Mater. 196 (1992) 347.
[42] F. Reimold, et al., Nucl. Fusion 55 (2015) 033004.
[43] J.L. Terry, et al., submitted to Nucl. Mater. and Energy (2016).
[44] J.R. Harrison, et al., J. Nucl. Mater. 463 (2015) 757.
[45] C.S. Change, et al., Phys. Plasmas 11 (2004) 2649.
[46] B. Dudson, et al., Computer Phys. Comm. 180 (2009) 1467.
[47] D. Stotler, et al., Nucl. Mater. and Energy. submitted to (2016).
[48] B. Dudson, et al., Developments in the Simulation of Turbulence and Neutral Gas with BOUT++, APS-DPP Meeting Abstracts, 2014.
[49] M. Greenwald, Phys. Plasmas 17 (2010) 058101.
[50] B. LaBombard, et al., Nucl. Fusion 55 (2015) 053020.
[51] A. Kallenbach, et al., Nucl. Fusion 52 (2012) 122003.